Unique Signatures of Topological Phases in Two-Dimensional THz Spectroscopy

Felix Gerken[®], ^{1,2} Thore Posske[®], ^{1,2} Shaul Mukamel[®], ³ and Michael Thorwart[®], ¹I. Institut für Theoretische Physik, Universität Hamburg, Notkestraße 9, 22607 Hamburg, Germany ²The Hamburg Centre for Ultrafast Imaging, Luruper Chaussee 149, 22761 Hamburg, Germany ³Departments of Chemistry and Physics and Astronomy, University of California, Irvine, California 92697-2025, USA

(Received 14 September 2021; revised 12 January 2022; accepted 3 June 2022; published 27 June 2022)

We develop a microscopic theory for the two-dimensional (2D) spectroscopy of one-dimensional topological superconductors. We consider a ring geometry of an archetypal topological superconductor with periodic boundary conditions, bypassing energy-specific differences caused by topologically protected or trivial boundary modes that are hard to distinguish. We show numerically and analytically that the cross-peak structure of the 2D spectra carries unique signatures of the topological phases of the chain. Our work reveals how 2D spectroscopy can identify topological phases in bulk properties.

DOI: 10.1103/PhysRevLett.129.017401

Topological phases of matter have attracted considerable attention following the discovery of topologically nontrivial magnetic and electronic phenomena like the Berezinskii-Kosterlitz-Thouless transition [1-4] and the integer and fractional quantum Hall effect [5.6]. Some topological systems, such as superconducting quantum wires [7], spin liquids [8], and vortices on surfaces of topological superconductors [9] are predicted to host anyons such as spatially isolated Majorana zero-energy boundary modes that are of interest to quantum information processing [10,11]. Despite experimental evidence of zeroenergy modes [12], their topological origin remains inconclusive [13]. Experimental techniques that reliably identify one-dimensional (1D) topological superconductors are badly needed. Current approaches detect the localized zero-energy boundary modes, but cannot unambiguously discriminate them against topologically trivial features that appear close to zero energy as well, like Yu-Shiba-Rusinov states [14–18], Kondo peaks [19,20], Andreev bound states [21], and Caroli-de Gennes-Matricon states [22,23]. In 2D electronic systems, dispersive Majorana edge modes have been shown to increase the linear optical conductivity [24].

A versatile advanced tool is nonlinear 2D spectroscopy [25,26] applied in the THz frequency regime to probe electronic excitations in solid-state nanostructures [27–30] or the Fermi glass phase in disordered correlated materials [31]. Recently, 2D spectroscopy of two- and three-dimensional topological spin liquids has theoretically revealed characteristic spectral properties of itinerant spin-based anyons and fractons [32–34] and of strongly correlated two-band Fermi-Hubbard models [35]. It offers additional features in comparison to pump-probe THz spectroscopy [36–39]. The main difference lies in the decoupling of the waiting time and excitation frequency resolution both of which are high [40]. This is in stark contrast to pump-probe spectroscopy where both are

inherently connected by a Fourier uncertainty. Moreover, the lack of large background signals permits excellent signal-to-noise ratios.

In this Letter, we employ 2D nonlinear spectroscopy to analyze the periodic Kitaev chain, the archetype of onedimensional topological superconductors, describing the topological electronic properties of nanowires [12], atomic magnetic chains [41,42], and cold atom systems [43]. Rather than investigating the Majorana boundary modes of this model, we consider a periodic configuration to study the topological properties of the bulk and characterize its two phases by 2D spectroscopy. This could be realized by atomic chain quantum corrals. In particular, we compare Kitaev chains with the same bulk energy spectrum but a different topological phase. We predict experimental signatures due to topological effects, eliminating differences caused solely by the bulk energy spectra or topologically trivial or nontrivial localized zero-energy states. We find signatures of superconducting topological band inversion in the 2D spectra, which are characteristic for the topological phase and which are absent in linear absorption spectra. Our predictions should be verifiable by 2D THz spectroscopy [27–31].

Model.—The Kitaev chain is a 1D spin-polarized unconventional superconductor with the Hamiltonian

$$H = \sum_{n=1}^{N} \left[-w a_{n+1}^{\dagger} a_n - \mu a_n^{\dagger} a_n + \Delta a_n a_{n+1} \right] + \text{H.c.}, \quad (1)$$

where a_n is a fermionic annihilation operator, 2μ is the chemical potential, w the nearest-neighbor hopping, and Δ is the complex superconducting gap parameter [7]. In physical systems, the parameters can assume a wide range of energies starting from suspended hybridizing atomic chains or semiconductors where they are of the order of eV

and going down to meV in hybridized Yu-Shiba-Rusinov states [12,44]. However, the superconducting gap is always in the meV range or less. The system has an electronic band gap for $|w| \neq |\mu|$ and $\Delta \neq 0$ [7]. For dominant hopping $|w| > |\mu|$, the open chain, i.e., $a_{N+1} = 0$, has an in-gap mode localized at both ends of the chain. Its energy is exponentially small in the system size. In the large-N limit, this mode decomposes into two spatially isolated Majorana operators [7] whose existence is protected by the electronic energy gap in the bulk. The mode can only disappear by closing the gap. Hence, there are two distinct gapped phases: the topologically trivial phase without and the topologically nontrivial phase with Majorana end modes. Both are characterized by a \mathbb{Z}_2 topological invariant of the bulk only [45,46]. The boundary modes are due to an interface between different topological phases explained by the bulk boundary correspondence [47].

Kitaev [7] has already pointed out that there is a map in form of a simple parameter transformation that leaves the band structure of the periodic chain invariant but changes the topological phase. We find that the transformed parameters are given by

$$\mu' = \pm w, \quad w' = \pm \mu, \quad \Delta' = e^{i\theta} \sqrt{\mu^2 + |\Delta|^2 - w^2},$$
 (2)

where ϑ is an arbitrary real number. If the system is originally in the nontrivial phase, i.e., $|\mu| < |w|$, then the transformed chain with the primed parameters will be in the trivial phase, because $|w'| = |\mu| < |w| = |\mu'|$. The same holds vice versa. By this, a dual Hamiltonian with the same spectrum but the inverse topological phase is assigned to each topologically trivial one. Yet, if $\mu^2 + |\Delta|^2 - w^2 < 0$, which can only happen in the nontrivial phase, there will be no trivial Hamiltonian with the same band structure.

We start with the simplest case, $w = \Delta$. The linear transformation U defined by

$$U^{\dagger} a_n U = i(a_n^{\dagger} - a_n - a_{n+1}^{\dagger} - a_{n+1})/2 \tag{3}$$

corresponds to the transformed parameters $\mu' = w$ and $w' = \Delta' = \mu$. In general, we can construct the map between the phases by concatenating the Bogoliubov transformation diagonalizing the trivial Hamiltonian with the inverse of the transformation that diagonalizes the nontrivial Hamiltonian with the same band structure. Even simpler, the map in Eq. (3) can be extended to $|w| \leq |\Delta|$ by fixing the superconducting phase to $\varphi = \arccos(w/|\Delta|)$.

2D spectroscopy.—In 2D spectroscopy, the system is subjected to three consecutive electromagnetic pulses and its response is probed by interference with a fourth pulse [25,26]. In the dipole approximation, i.e., when the shortest wavelength of the light is much larger than the extent of the chain, the radiation-matter interaction Hamiltonian reads $V(t) = -d \cdot E(t)$, where d denotes the dipole operator and E(t) the electric field. For the Kitaev chain, d = -eR with

the position operator $\mathbf{R} = \sum_{n=1}^{N} \mathbf{r}_n a_n^{\dagger} a_n$ and e the electron charge. Here, \mathbf{r}_n is the location of site n. We consider a ring of radius r with $\mathbf{r}_n = r(\cos(2\pi n/N), \sin(2\pi n/N), 0)^T$. A similar dipole operator emerges from a low-energy description of realistic systems as shown for a Rashba wire in the Supplemental Material [48].

We are interested in the time-dependent polarization $P(t) = \langle d(t) \rangle_{\rho(t)}$, which provides the measurable electromagnetic response. Here, $\rho(t)$ is the density matrix of matter. Because the system consists of broad electronic bands, we compute the full third-order signal $P^{(3)}(t)$ for the 2D spectra, which is the sum of all phase matching directions. It can be detected in a collinear beam geometry. Breaking it into phase matching components could reveal additional information on specific groups of dynamical pathways, which goes beyond the present study. Coherent 2D techniques, in particular the double quantum coherence, are usually applied to discrete electronic systems like molecules [49].

We assume that at time t = 0 the system is in its ground state, and obtain the third-order contribution to the polarization [25,26]

$$P^{(3),j}(t) = \int_0^\infty dt_3 dt_2 dt_1 E^m(t - t_3) E^l(t - t_3 - t_2)$$

$$\times E^k(t - t_3 - t_2 - t_1) S_{klm}^{(3),j}(t_3, t_2, t_1), \tag{4}$$

with a sum over repeated indices and the third-order response function $S_{klm}^{(3),j}(t_3,t_2,t_1)$. The 2D signal is displayed by its Fourier transform

$$S_{klm}^{(3),j}(\omega_3, t_2, \omega_1) = \frac{2}{\hbar^3} \theta(t_2) \sum_{\alpha=1}^4 \int_0^\infty \int_0^\infty \text{Im} C_{\alpha, klm}^j(t_3, t_2, t_1) \times e^{i(\omega_1 t_1 + \omega_3 t_3)} dt_1 dt_3,$$
 (5)

with the Heaviside function $\theta(t)$ and C_{α} are the four-point correlation functions of the dipole operator (see the Supplemental Material [48]). ω_1 and ω_3 are the excitation and detection frequency, respectively, and t_2 the waiting time. In the following, we set $t_2 = 0$.

Results.—We restrict the discussion to the $S_{xxx}^{(3),x}$ component, where all light pulses are polarized in the x direction. The signals for this feasible configuration are similar to the ones for a physically unrealistic linear chain with periodic boundary conditions. We choose a representative slice in the $(w = \Delta)$ plane to demonstrate the parameter dependence of the 2D spectra. By this, we can use the map in Eq. (3) to clarify the qualitative differences between the phases. Representatives of the two phases are the trivial atomistic limit (dissected atoms) and the sweet spot of the Majorana chain that hosts localized Majorana modes in an open chain. We fix the maximal quasiparticle energy Λ as the energy scale. In our case, Λ can be in the meV regime, but depending on the physical system, Λ can vary up to eV [12,44]. We follow the trajectory

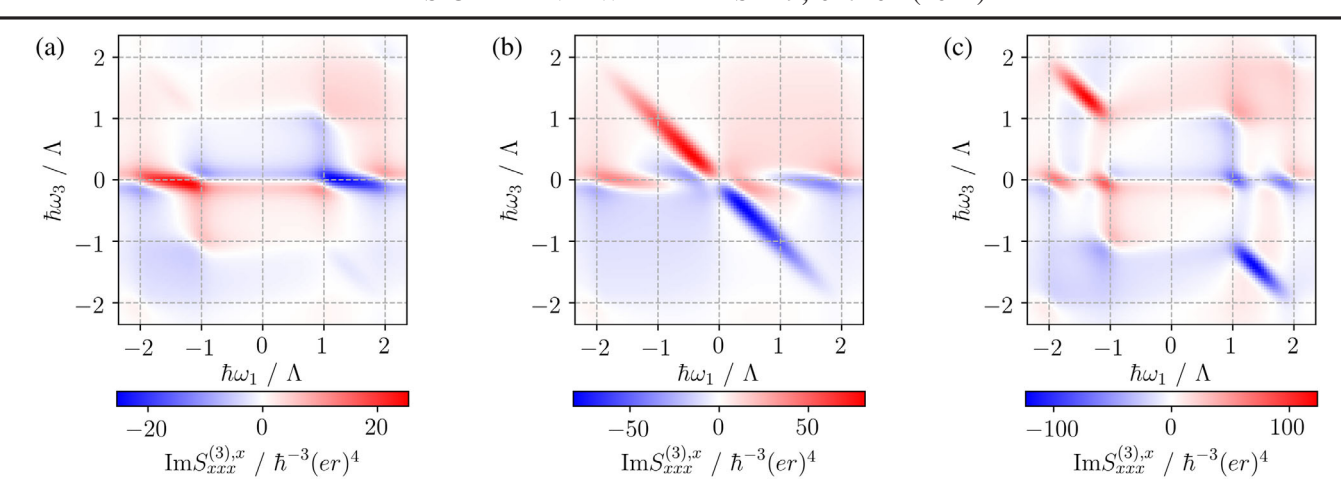


FIG. 1. Imaginary part of the 2D spectrum of the Kitaev ring at waiting time $t_2 = 0$ (a) in the topologically trivial phase with $\mu = 0.375\Lambda$, $w = \Delta = 0.125\Lambda$, (b) at the critical point in between with $\mu = 0.25\Lambda$, $w = \Delta = 0.25\Lambda$, and (c) in the nontrivial phase with $\mu = 0.125\Lambda$, $w = \Delta = 0.375\Lambda$. The chain length is N = 60, Λ is the maximal excitation energy of a single quasiparticle. The topologically trivial and nontrivial phases are distinguished by peaks on the counterdiagonal and the splitting of the peak on the horizontal.

$$\Gamma_s = (\mu_s, w_s, \Delta_s) = \Lambda(1 - s, s, s)/2, \tag{6}$$

where $0 \le s \le 1$, which interpolates between the two extreme cases $H(\Gamma_0)$ being the Hamiltonian in the atomistic limit and $H(\Gamma_1)$ the Hamiltonian for the sweet spot, such that Λ remains unchanged at all instances. For s < 0.5, $H(\Gamma_s)$ is in the topologically trivial phase, for s > 0.5 in the nontrivial phase, and for s = 0.5, the system reaches the semimetallic critical point, where the bulk gap closes. The spectra and band structures of $H(\Gamma_s)$ and $H(\Gamma_{1-s})$ coincide due to the map U in Eq. (3). By this, 2D spectra for different topological phases with the same eigenenergies can be compared.

Representative 2D spectra for a band gap of $\Lambda/2$ and for the gapless critical point are shown in Fig. 1 (see also the Supplemental Movie [48]). They include a Gaussian broadening ($\sigma = 0.05\Lambda$) to increase readability. Noticeable peaks in the 2D spectra are arranged along three main axes, the diagonal $\omega_1 = \omega_3$, the counterdiagonal $\omega_1 = -\omega_3$, and the horizontal $\omega_3 = 0$. Valuable information is contained in

the cross peaks on the counterdiagonal and the horizontal. A change of the cross-peak pattern is observed when passing from the topologically trivial to the nontrivial phase. The counterdiagonal peaks dominate the nontrivial phase, while they almost disappear in the trivial phase. The horizontal peaks appear in both phases. They form a large inhomogeneously broadened peak in the trivial phase but become disconnected in the nontrivial phase and are most pronounced at the band edges. Furthermore, their relative magnitude significantly decreases. In general, the overall magnitude of the 2D spectra increases for $s \to 1$. The peak amplitudes between the phases differ by orders of magnitude. For perfectly flat bands in the trivial phase, they can even vanish due to the charge conserving nature of the dipole operator. The ground state in the trivial phase with flat bands is either the empty or fully filled lattice. There are no other states with the same charge, hence, all transitions are forbidden. For flat bands in the nontrivial phase, there are numerous possible transitions, in contrast. The charge expectation value of the ground state is -Ne/2. We estimate

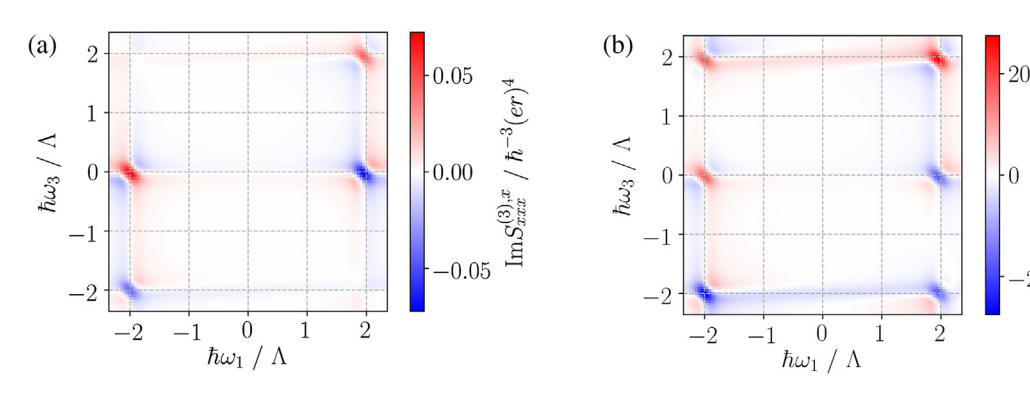
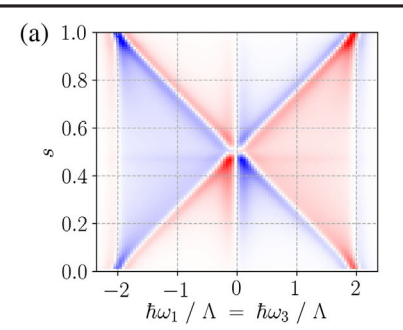
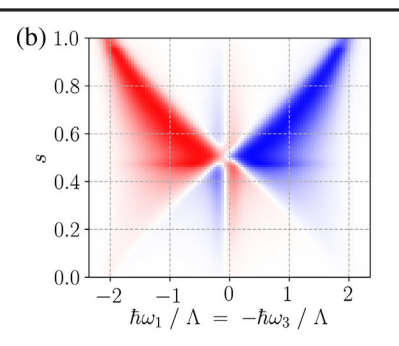


FIG. 2. Imaginary part of the 2D spectrum of the Kitaev ring in (a) the topologically trivial phase with $\mu = 0.005\Lambda$, $w = \Delta = 0.495\Lambda$, and (b) the nontrivial phase with $\mu = 0.495\Lambda$ and $w = \Delta = 0.005\Lambda$ for N = 60.





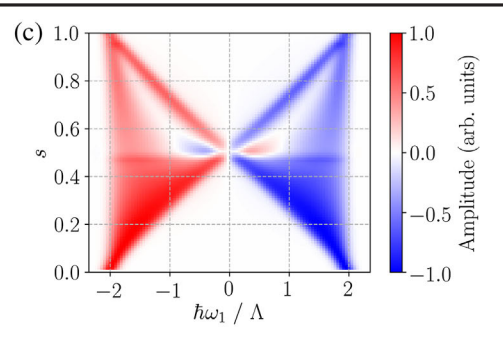


FIG. 3. (a) Diagonal, (b) counterdiagonal, and (c) horizontal sections of the imaginary part of the 2D spectra for the Hamiltonian $H(\Gamma_s)$ as a function of s following Eq. (6). For each parameter set Γ_s , the 2D spectra are normalized to their maximal peak amplitude. The chain length is N=60. Differences between the topological phases emerge along the counterdiagonal and the horizontal lines. In the trivial phase (s<0.5), the counterdiagonal peaks disappear. The horizontal peaks are more pronounced in the trivial phase than in the nontrivial phase (s>0.5).

that for even N, the number of Fock states with charge -Ne/2 is $2^N/\sqrt{N}$ due to Sterling's formula. This accounts for the discrepancy of the magnitudes between the 2D spectra of the almost flat band scenarios shown in Fig. 2.

For the nearly flat bands in Fig. 2, we find essential differences between the 2D spectra of the two topological phases. In the trivial phase, the horizontal peaks are the dominant cross peaks while counterdiagonal peaks are absent. In the nontrivial phase, the counterdiagonal peaks are dominant while the horizontal peaks are reduced. To show that this is generic, we depict the cross sections along the diagonal, counterdiagonal, and horizontal in Fig. 3. For each value of s, the 2D spectra are normalized to their maximal peak amplitude. The diagonal at $t_2 = 0$ carries information on the linear response spectra. We find the 2D spectra to be symmetric about the phase transition at s = 0.5. This reaffirms that the linear response cannot uncover differences between the phases. Our analytic calculations show that the difference between the phases in linear spectroscopy is essentially a scaling factor [48]. For the counterdiagonal, cross peaks disappear in the trivial regime s < 0.5, but are strong in the nontrivial regime s > 0.5. Importantly, the change in the relative peak amplitudes when crossing the critical point s = 0.5 is continuous. The signal from the horizontal sections forms a broad continuum in the trivial phase that is clearly split in the topological phase. This is caused by the superconducting topological band inversion characteristic for the model. The anomalous term in Eq. (1) mixes the particle and hole bands. In the trivial phase, the bands maintain their predominant particle and hole character, respectively. In the topological phase, the bands change between particle and hole character at the inversion points in the Brillouin zone. There, the nonvanishing two-particle to two-particle transition dipole moments have a gap closure [48]. This is absent in the trivial phase and is thus unique to the topological phase. For large N, their transition frequencies go to zero. Hence, they contribute to the horizontal peaks in the 2D spectra, and the observed splitting of the peak continua provides a clear signature of the superconducting topological band inversion. The difference in the cross peaks and the absence of any difference in the diagonal peaks are a fundamental advantage of nonlinear spectroscopy for characterizing topological phases. Our results transfer to finite Kitaev chains with open boundary conditions. Yet, additional Majorana end modes as well as possible trivial zero-energy modes result in a doubling of the 2D spectrum at energies of the order of the band gap that must be accounted for. Remarkably, the bulk contribution is qualitatively the same as for the periodic configuration, suggesting that our results are largely insensitive to the specific geometry underlying the dipole operator. Furthermore, local parametric disorder of up to 30% of the band gap energy does not significantly affect the signature of the topological phase. These two observations suggest the robustness of the signature of the topological phase (see the Supplemental Material [48] for more details).

The map U offers an alternative interpretation of our results. Rather than considering U to actively change the topological phase, we could equivalently consider the Hamiltonian to be invariant and passively transform the measurement operator, i.e., the dipole operator, which has the form of a local chemical potential, into the Majorana braiding operator $B_{n,n+1} = a_{n+1}^{\dagger} a_n + a_{n+1} a_n + \text{H.c.}$ for adjacent sites [50]. Formally, this means $U^{\dagger}dU = (e/2) \sum_{n=1}^{N} \mathbf{r}_n B_{n,n+1}$. Then, the 2D spectrum can be interpreted in two ways: first, the chain being in one phase and probed by the common dipole operator, and second the chain being in the other phase and probed by the braiding operator.

Conclusions.—With the Kitaev ring, we propose a physical realization of the Kitaev chain with periodic boundary conditions and calculate the THz response in 2D nonlinear spectroscopy with three parallel polarized field pulses. By a mapping between the topologically trivial and nontrivial phases that changes the phase but not the band structure of the Kitaev Hamiltonian, we identify signatures stemming solely from topological effects and

not from the energy spectra. A superconducting topological band inversion is then detected by cross peaks in the 2D spectra, which underlines the advantage of nonlinear spectroscopy over linear spectroscopy for topological systems. A band inversion has recently been resolved in scanning tunneling microscope experiments [44], which couples to the local charge rather than the dipole operator. 2D spectroscopy is less invasive, offers higher spectral resolution, and is less prone to dissipation, where any backaction of a macroscopic tip on the quantum system can be excluded. A seeming caveat of our approach is that the superconducting gap Δ should be rather large for the Umap to exist. However, our analytic computation of the dipole moments [48] suggests that our results carry over to small Δ . In contrast to topological spin liquids [32,33], the electronic system at hand can be probed both in its topologically trivial and nontrivial phase, and its topological features are revealed by bulk properties only, omitting the spectroscopy of hard-to-control low-energy topological quasiparticles that interfere with the topological response of the bulk. Future research on multiple topological band inversions and multiband models could help to establish a general connection between our findings and the bulk topological invariant.

We thank Hong-Guang Duan for helpful discussions. M. T. and F. G. acknowledge support by the Cluster of Excellence "CUI: Advanced Imaging of Matter" of the Deutsche Forschungsgemeinschaft (DFG)—EXC 2056—project ID 390715994. T. P. acknowledges funding by the Deutsche Forschungsgemeinschaft (DFG) project no. 420120155. S. M. gratefully acknowledges the support of the National Science Foundation Grant CHE-1953045.

- [1] V. L. Berezinskii, Sov. Phys. JETP **32**, 493 (1971), http://www.jetp.ras.ru/cgi-bin/e/index/e/32/3/p493?a=list.
- [2] V. L. Berezinskii, Sov. Phys. JETP **34**, 610 (1972), http://www.jetp.ras.ru/cgi-bin/e/index/e/34/3/p610?a=list.
- [3] J. M. Kosterlitz and D. J. Thouless, J. Phys. C 5, L124 (1972).
- [4] J. M. Kosterlitz and D. J. Thouless, J. Phys. C 6, 1181 (1973).
- [5] K. v. Klitzing, G. Dorda, and M. Pepper, Phys. Rev. Lett. 45, 494 (1980).
- [6] D. C. Tsui, H. L. Störmer, and A. C. Gossard, Phys. Rev. Lett. 48, 1559 (1982).
- [7] A. Kitaev, Phys. Usp. 44, 131 (2001).
- [8] A. Kitaev, Ann. Phys. (Amsterdam) 321, 2 (2006).
- [9] L. Fu and C. L. Kane, Phys. Rev. Lett. **100**, 096407 (2008).
- [10] C. Nayak, S. H. Simon, A. Stern, M. Freedman, and S. Das Sarma, Rev. Mod. Phys. 80, 1083 (2008).
- [11] J. Alicea, Y. Oreg, G. Refael, F. von Oppen, and M. P. A. Fisher, Nat. Phys. 7, 412 (2011).
- [12] V. Mourik, K. Zuo, S. M. Frolov, S. R. Plissard, E. P. A. M. Bakkers, and L. P. Kouwenhoven, Science 336, 1003 (2012).

- [13] H. Zhang et al., Nature (London) **591**, E30 (2021).
- [14] L. Yu, Acta Phys. Sin. 114, 75 (1965).
- [15] H. Shiba, Prog. Theor. Phys. 40, 435 (1968).
- [16] A. I. Rusinov, JETP Lett. 9, 85 (1969), http://jetpletters.ru/ ps/1658/article_25295.shtml.
- [17] B. W. Heinrich, J. I. Pascual, and K. J. Franke, Prog. Surf. Sci. 93, 1 (2018).
- [18] L. Cornils, A. Kamlapure, L. Zhou, S. Pradhan, A. A. Khajetoorians, J. Fransson, J. Wiebe, and R. Wiesendanger, Phys. Rev. Lett. 119, 197002 (2017).
- [19] E. Müller-Hartmann and J. Zittartz, Phys. Rev. Lett. 26, 428 (1971).
- [20] C. P. Moca, I. Weymann, M. A. Werner, and G. Zaránd, Phys. Rev. Lett. 127, 186804 (2021).
- [21] P. Yu, J. Chen, M. Gomanko, G. Badawy, E. P. A. M. Bakkers, K. Zuo, V. Mourik, and S. M. Frolov, Nat. Phys. 17, 482 (2021).
- [22] C. Caroli, P. de Gennes, and J. Matricon, Phys. Lett. 9, 307 (1964).
- [23] D. Wang, L. Kong, P. Fan, H. Chen, S. Zhu, W. Liu, L. Cao, Y. Sun, S. Du, J. Schneeloch, R. Zhong, G. Gu, L. Fu, H. Ding, and H.-J. Gao, Science 362, 333 (2018).
- [24] J. J. He, Y. Tanaka, and N. Nagaosa, Phys. Rev. Lett. 126, 237002 (2021).
- [25] S. Mukamel, *Principles of Nonlinear Optics and Spectroscopy* (Oxford University Press, New York, 1995).
- [26] L. Valkunas, D. Abramavicius, and T. Mančal, *Molecular Excitation Dynamics and Relaxation* (Wiley-VCH, Weinheim, 2013).
- [27] W. Kuehn, K. Reimann, M. Woerner, T. Elsaesser, and R. Hey, J. Phys. Chem. B 115, 5448 (2011).
- [28] M. Woerner, W. Kuehn, P. Bowlan, K. Reimann, and T. Elsaesser, New J. Phys. 15, 025039 (2013).
- [29] G. Nardin, Semicond. Sci. Technol. 31, 023001 (2016).
- [30] S. Markmann, M. Franckié, S. Pal, D. Stark, M. Beck, M. Fiebig, G. Scalari, and J. Faist, Nanophotonics 10, 171 (2021).
- [31] F. Mahmood, D. Chaudhuri, S. Gopalakrishnan, R. Nandkishore, and N. P. Armitage, Nat. Phys. 17, 627 (2021).
- [32] W. Choi, K. H. Lee, and Y. B. Kim, Phys. Rev. Lett. **124**, 117205 (2020).
- [33] R. M. Nandkishore, W. Choi, and Y. B. Kim, Phys. Rev. Research 3, 013254 (2021).
- [34] Y. Wan and N. P. Armitage, Phys. Rev. Lett. **122**, 257401 (2019).
- [35] N. T. Phuc and P. Q. Trung, Phys. Rev. B 104, 115105 (2021).
- [36] T. Elsaesser, K. Reimann, and M. Woerner, *Concepts and Applications of Nonlinear Terahertz Spectroscopy* (Morgan & Claypool Publishers, San Rafael, 2019).
- [37] J. Lu, X. Li, Y. Zhang, H. Y. Hwang, B. K. Ofori-Okai, and K. A. Nelson, Top. Curr. Chem. 376, 6 (2018).
- [38] R. Ulbricht, E. Hendry, J. Shan, T. F. Heinz, and M. Bonn, Rev. Mod. Phys. **83**, 543 (2011).
- [39] S.-H. Shima and M. T. Zanni, Phys. Chem. Chem. Phys. 11, 748 (2009).
- [40] A. Gelzinis, R. Augulis, V. Butkus, B. Robert, and L. Valkunas, Biochim. Biophys. Acta **1860**, 271 (2019).
- [41] S. Nadj-Perge, I. K. Drozdov, J. Li, H. Chen, S. Jeon, J. Seo, A. H. MacDonald, B. A. Bernevig, and A. Yazdani, Science **346**, 602 (2014).

- [42] H. Kim, A. Palacio-Morales, T. Posske, L. Rózsa, K. Palotás, L. Szunyogh, M. Thorwart, and R. Wiesendanger, Sci. Adv. 4, eaar5251 (2018).
- [43] J. Ruhman, E. Berg, and E. Altman, Phys. Rev. Lett. **114**, 100401 (2015).
- [44] L. Schneider, P. Beck, T. Posske, D. Crawford, E. Mascot, S. Rachel, R. Wiesendanger, and J. Wiebe, Nat. Phys. 17, 943 (2021).
- [45] A. Kitaev, AIP Conf. Proc. 1134, 22 (2009).
- [46] Note that the Kitaev chain possesses an artificial timereversal symmetry and is therefore in the Cartan-Altland-Zirnbauer class BDI with a \mathbb{Z} invariant. However, this

- symmetry is broken by realistic perturbations. Hence, we consider the system to be in class D.
- [47] A. M. Essin and V. Gurarie, Phys. Rev. B 84, 125132 (2011).
- [48] See Supplemental Material at http://link.aps.org/supplemental/10.1103/PhysRevLett.129.017401 for further details and Supplemental Movie 1 for the 2D spectra as the system parameters vary. The spectra in the movie are normalized to the maximal peak amplitude for each set of parameters.
- [49] D. Abramavicius, B. Palmieri, D. V. Voronine, F. Šanda, and S. Mukamel, Chem. Rev. 109, 2350 (2009).
- [50] D. A. Ivanov, Phys. Rev. Lett. 86, 268 (2001).

Supplemental Material

Unique Signatures of Topological Phases in Two-Dimensional THz Spectroscopy

Felix Gerken, ^{1, 2} Thore Posske, ^{1, 2} Shaul Mukamel, ³ and Michael Thorwart ^{1, 2}

¹I. Institut für Theoretische Physik, Universität Hamburg, Notkestraße 9, 22607 Hamburg, Germany

² The Hamburg Centre for Ultrafast Imaging, Luruper Chaussee 149, 22761 Hamburg, Germany

³ Departments of Chemistry and Physics & Astronomy,

University of California, Irvine, California 92697-2025, USA

In this Supplemental Material, we give the explicit expressions for the 4-point correlation functions contributing to the third-order response function of the Kitaev chain. We provide details of the numerical evaluation of the correlation functions. The many-particle transition dipole moments are computed numerically and complemented by analytic results for the large-N limit. Furthermore, we show that our results for the Kitaev ring model carry over to the more realistic model of a Rashba wire. We conclude by discussing the effect of disorder on our results.

I. CORRELATION FUNCTIONS

The third-order response function is given by

$$S_{klm}^{(3),j}(t_3, t_2, t_1) = \frac{2}{\hbar^3} \theta(t_1) \theta(t_2) \theta(t_3) \sum_{\alpha=1}^4 \operatorname{Im} C_{\alpha, klm}^j(t_3, t_2, t_1)$$
(S1)

with the Heaviside step function $\theta(t)$. The four-point correlation functions C_{α} are given by

$$C_{1,klm}^{j}(t_3, t_2, t_1) = \langle d_l(t_1) d_m(t_1 + t_2) d^j(t_1 + t_2 + t_3) d_k(0) \rangle_{\rho},$$
 (S2)

$$C_{2,klm}^{j}(t_3, t_2, t_1) = \langle d_k(0)d_m(t_1 + t_2)d^j(t_1 + t_2 + t_3)d_l(t_1)\rangle_{\rho},$$
(S3)

$$C_{3,klm}^{j}(t_3, t_2, t_1) = \langle d_k(0)d_l(t_1)d^j(t_1 + t_2 + t_3)d_m(t_1 + t_2)\rangle_{\rho},$$
(S4)

$$C_{4,klm}^{j}(t_{3},t_{2},t_{1}) = \langle d^{j}(t_{1}+t_{2}+t_{3}) d_{m}(t_{1}+t_{2}) d_{l}(t_{1}) d_{k}(0) \rangle_{\rho}.$$
 (S5)

Here, d_j is the j-th component of the dipole operator **d** and ρ is the groundstate of the unperturbed system. For a derivation of these expression, we are referring to Chapter 13 of Ref. [26] of the main text.

II. NUMERICAL EVALUATION OF THE CORRELATION FUNCTIONS

We find the eigenmodes of the Kitaev chain in momentum space by a standard Bogoliubov transformation [7] (main text), where we define all quasiparticle energies to be non-negative. The quasiparticle vacuum $|\Omega\rangle$ and the groundstate of the system then coincide. With this, the 4-point correlation functions for the x-components of the dipole operator are of the form

$$C = \langle \Omega | d_x(\tau_1) d_x(\tau_2) d_x(\tau_3) d_x(\tau_4) | \Omega \rangle. \tag{S6}$$

Consider a general quadratic operator for the dipole operator

$$d_{x}(\tau) = \sum_{i,j=1}^{N} \left[A_{ij}(\tau) f_{i}^{\dagger} f_{j} + B_{ij}(\tau) f_{i}^{\dagger} f_{j}^{\dagger} + C_{ij}(\tau) f_{i} f_{j} + D_{ij}(\tau) f_{i} f_{j}^{\dagger} \right]. \tag{S7}$$

The matrices A, B, C and D are obtained either numerically or analytically from the Bogoliubov transformation that diagonalizes the Hamiltonian. To compute the correlation functions, we insert Eq. (S7) into Eq. (S6). Evaluating the correlation functions reduces to computing the vacuum expectation values of products of creation and annihilation operators. We achieve this combinatorically involved task in a systematic way by using Wick contractions and Wick's theorem. The results are sums of traces of products of the matrices A, B, C and D at different times τ_1, τ_2, τ_3 and τ_4 that must be evaluated numerically.

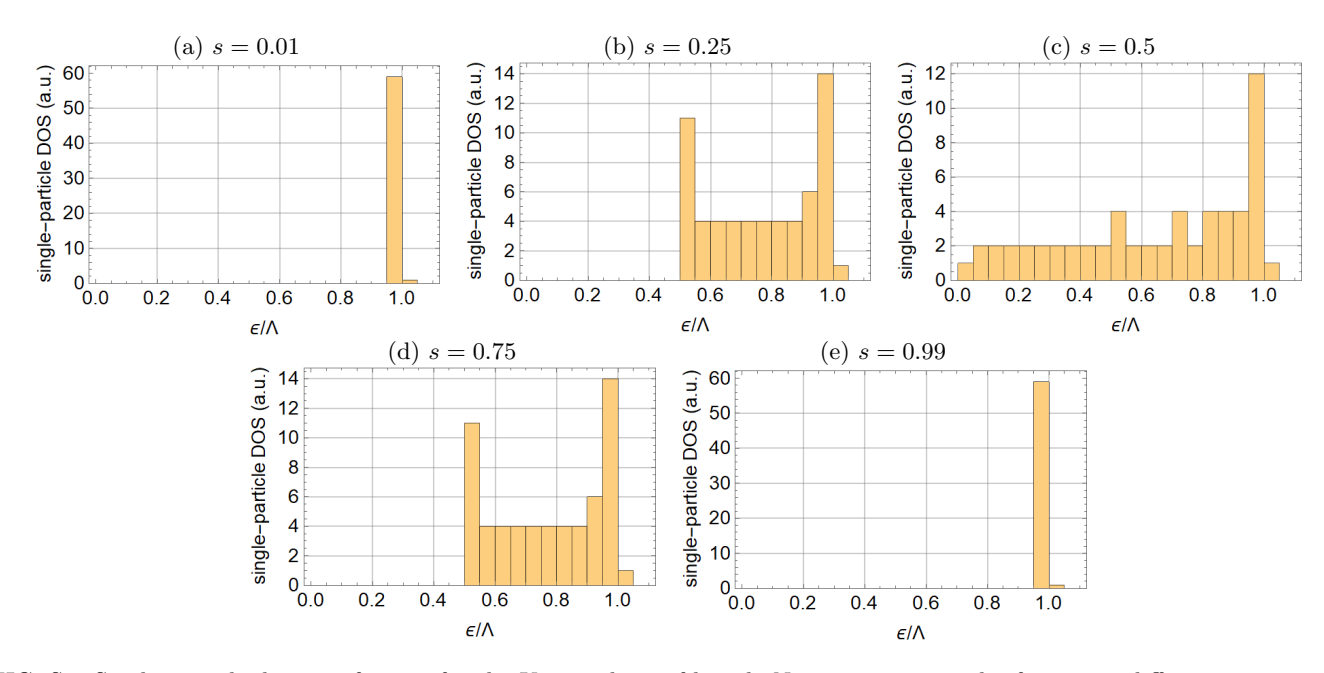


FIG. S1. Single-particle density of states for the Kitaev chain of length N=60 as a general reference at different parameters corresponding to $s=0.01,\,0.25,\,0.5,\,0.75,\,0.99$, respectively (see main text).

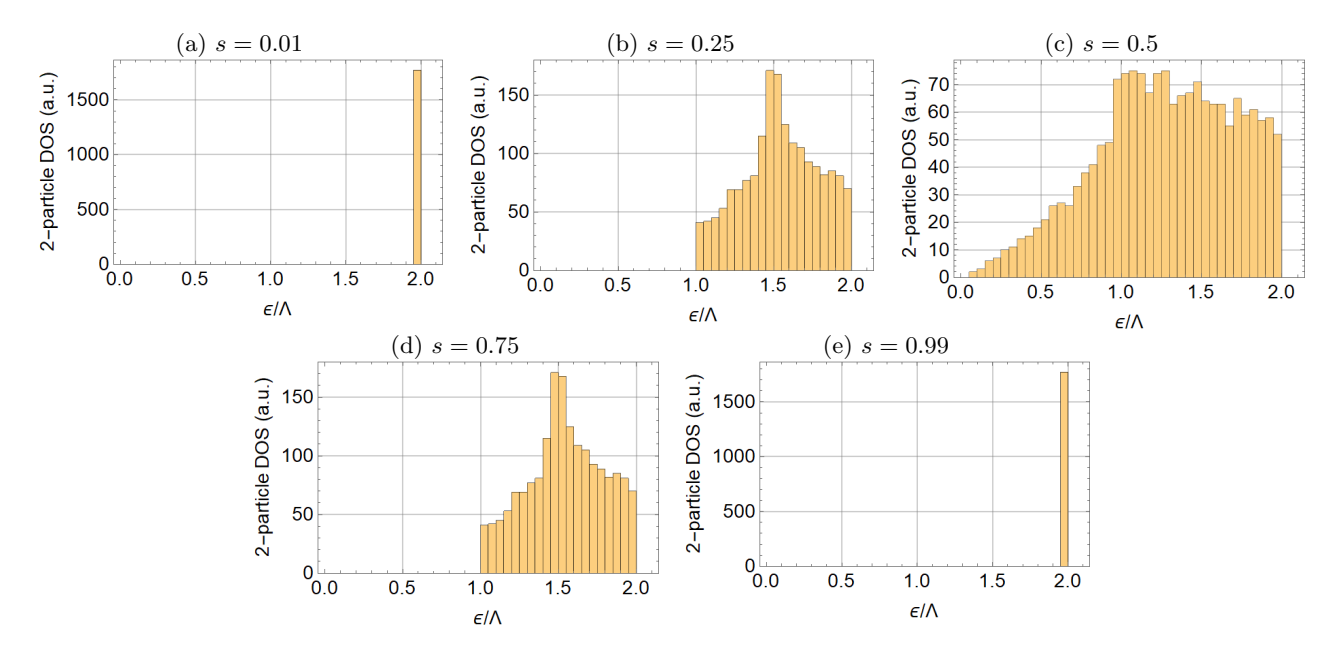


FIG. S2. Histograms of the two-particle density of states for chain length N=60.

III. DENSITY OF STATES AND THE DIPOLE OPERATOR MATRIX ELEMENTS

Here, we provide the density of states of two- and four-quasiparticle states as well as the corresponding matrix elements of the dipole operator ${\bf d}$. We constrain ourselves to its x-component, because the z-component vanishes by definition and the y-component carries equivalent information in the rotationally invariant system. We numerically construct the many-particle Fock states directly from the single-particle states of a Kitaev chain of length N=60 by standard combinatorics. In total, there are 1770 states with two quasiparticles and 487635 with four quasiparticles. The corresponding density of states is depicted in Figs. (S1-S3) for a representative choice of parameters s (see main text), which cover the topologically trivial phase at s < 0.5, the critical point at s = 0.5, and the nontrivial phase at s > 0.5.

We further evaluate the matrix elements of the x-component of the dipole operator numerically for two- and four-

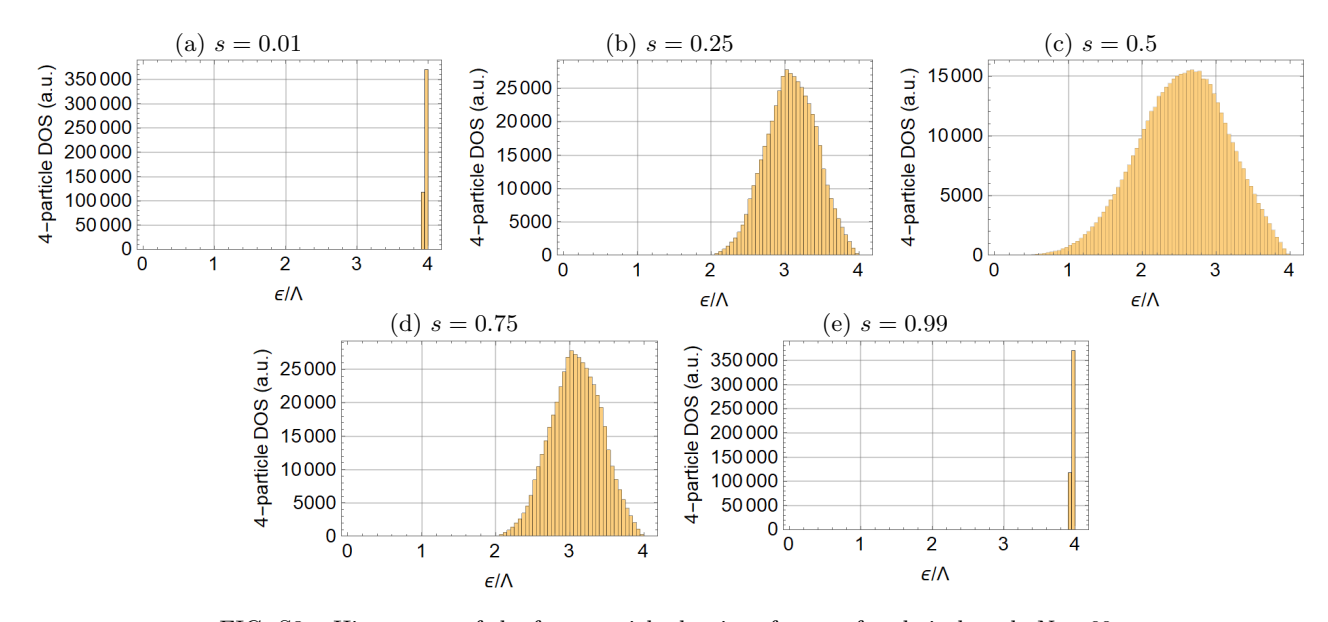


FIG. S3. Histograms of the four-particle density of states for chain length N=60.

particles cases. Between these states, the vast majority of matrix elements vanishes because the dipole operator either changes the number of quasiparticles by ± 2 or leaves the number of quasiparticles unchanged. Further matrix elements vanish because the dipole operator only combines momentum modes that are close-by. This is seen by expressing the dipole operator in momentum space, i.e.,

$$d_x = -eR \sum_j \cos\left(\frac{2\pi}{N}j\right) a_j^{\dagger} a_j = -\frac{eR}{2} \sum_k \tilde{a}_{k+1}^{\dagger} \tilde{a}_k + h.c., \tag{S8}$$

with the Fourier transformed quasiparticle operator \tilde{a}_k . The results are shown in Figs. (S4-S6), which depict the nonvanishing matrix elements $\Omega_{a,b}$ between states with a quasiparticle excitations and b quasiparticle excitations, where a and b are 0, 2, or 4. The matrix elements connecting the groundstate with two-particle states as well as the matrix elements that connect two-particle states to two-particle states represent the energetically lowest states where signatures of braiding of quasiparticles can occur. In fact, from $\Omega_{2,2}$, i.e., the dipole transitions between states with two quasiparticles, we observe a gap for the topologically trivial phase at s < 0.5, which is closed in the topologically nontrivial phase s > 0.5. As we elaborate in Secs. IV C 3 and V, the closure of the gap in $\Omega_{2,2}$ indicates a change of the character of an electronic band from particle-like to hole-like. This is a key feature of gapped topological phases of matter.

IV. ANALYTIC DETAILS AND DISCUSSION

A. Eigenmodes and Eigenenergies

First, we briefly summarize the solution of the Kitaev chain as given by Kitaev in his original paper from 2001, see Ref. [7] of the main text. The Hamiltonian of the periodic Kitaev chain is

$$H = \sum_{n=1}^{N} \left[-w a_{n+1}^{\dagger} a_n - \mu a_n^{\dagger} a_n + \Delta a_n a_{n+1} \right] + \text{h.c.},$$
 (S9)

with the hopping amplitude w, the chemical potential 2μ , and the complex superconducting gap parameter $\Delta = |\Delta|e^{i\varphi}$. Periodic boundary conditions are enforced by $a_{N+1} \equiv a_1$. The system is gauge invariant under the change of the superconducting phase φ . The Hamiltonian is diagonalized by the eigenmodes (Bogoliubons)

$$f_k = \begin{cases} e^{i(\frac{\pi}{4} + \frac{\varphi}{2})} \cos(\frac{\vartheta_k}{2}) \tilde{a}_k + e^{-i(\frac{\pi}{4} + \frac{\varphi}{2})} \sin(\frac{\vartheta_k}{2}) \tilde{a}_{-k}^{\dagger}, & \text{if } w \cos(\frac{2\pi}{N}k) + \mu > 0, \\ -e^{i(\frac{\pi}{4} + \frac{\varphi}{2})} \sin(\frac{\vartheta_k}{2}) \tilde{a}_k + e^{-i(\frac{\pi}{4} + \frac{\varphi}{2})} \cos(\frac{\vartheta_k}{2}) \tilde{a}_{-k}^{\dagger}, & \text{if } w \cos(\frac{2\pi}{N}k) + \mu < 0, \end{cases}$$
(S10)

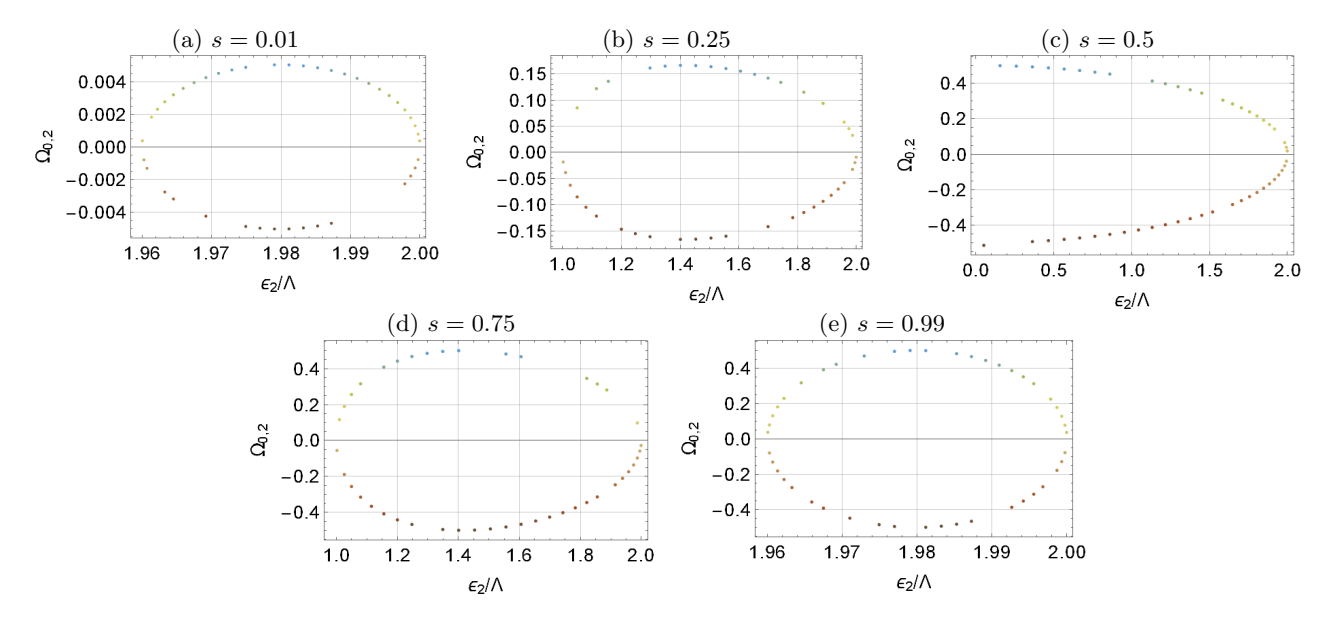


FIG. S4. Dipole matrix elements $\Omega_{0,2}$ between the ground state and states with two quasi-particles excitations and energy ϵ_2 .

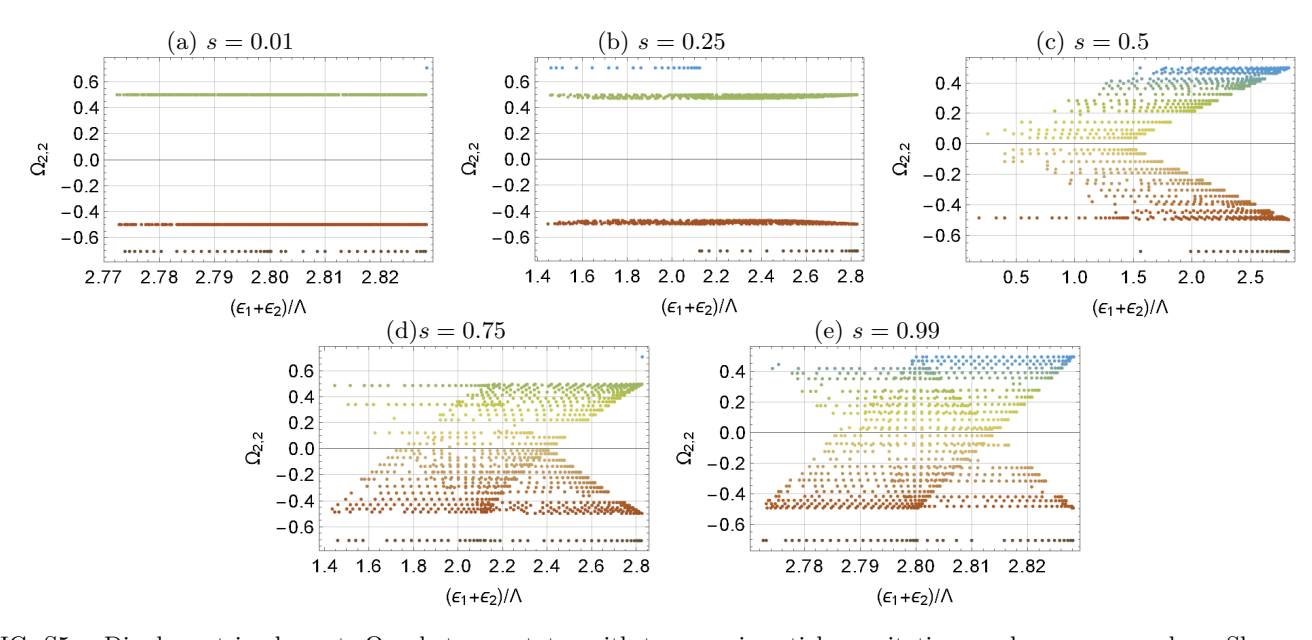


FIG. S5. Dipole matrix elements $\Omega_{2,2}$ between states with two quasi-particles excitations and energy ϵ_1 and ϵ_2 . Shown are the projections onto the $(\epsilon_1 + \epsilon_2)$ line. The $(\epsilon_1 - \epsilon_2)$ -dependence becomes irrelevant for long chains, as inferred by the analytic calculations. The gap closure in $\Omega_{2,2}$ shown for s = 0.75 and s = 0.99 marks an inversion of the band from particle to hole character, a key feature of a gapped topological phase, see analytical calculations and Sec. V.

with the Fourier transformed operators $\tilde{a}_k = (1/\sqrt{N}) \sum_{j=1}^N \exp\left(2\pi i j k/N\right) a_j$ and the mixing angle

$$\vartheta_k = \arctan\left(\frac{|\Delta|\sin\left(\frac{2\pi}{N}k\right)}{w\cos\left(\frac{2\pi}{N}k\right) + \mu}\right). \tag{S11}$$

The Bogoliubov transformation mixes particle and hole states. We can choose the Bogoliubov transformation to be orthogonal by gauge fixing $\varphi = -\pi/4$. The diagonalized Hamiltonian reads

$$H = \sum_{k=1}^{N} \epsilon_k \left(f_k^{\dagger} f_k - \frac{1}{2} \right) = \sum_{k=1}^{N} \frac{\epsilon_k}{2} \left(f_k^{\dagger} f_k - f_k f_k^{\dagger} \right), \tag{S12}$$

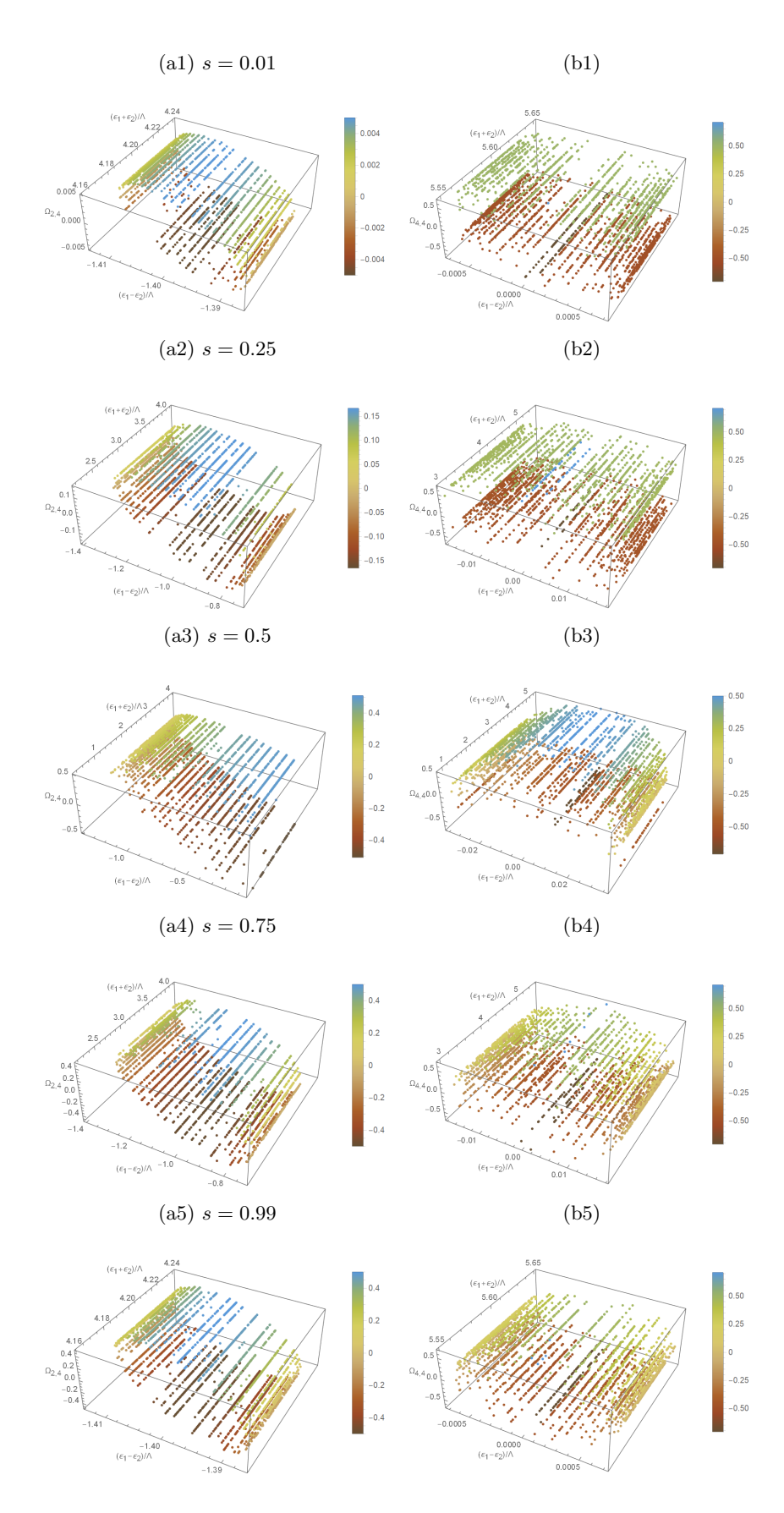


FIG. S6. The dipole matrix elements $\Omega_{a,b}$ between states with two and four quasiparticle excitations. Each diagram includes 100,000 uniformly randomly drawn pairs of states at energies ϵ_1 and ϵ_2 (measured as differences from the ground state energy) and their corresponding matrix elements. The parameter s takes on the values 0.01, 0.25, 0.5, 0.75, and 0.99 from top to bottom.

with the dispersion relation [7] (main text)

$$\epsilon_k = 2\sqrt{\left(w\cos\left(\frac{2\pi}{N}k\right) + \mu\right)^2 + |\Delta|^2\sin^2\left(\frac{2\pi}{N}k\right)}.$$
 (S13)

Note that for $|w| < |\mu|$, the eigenmodes have either predominantly particle or predominantly hole character depending on the sign of the chemical potential. For $|w| > |\mu|$ and $\Delta \neq 0$, there are distinct k-regions with particle and with hole character. The change from particle to hole character happens at the inversion points $\frac{2\pi}{N}k_{\text{inv}} = \arccos\left(\frac{-\mu}{w}\right)$ and $\frac{2\pi}{N}(-k_{\text{inv}}) \equiv 2\pi - \frac{2\pi}{N}k_{\text{inv}}$. These relations distinguish two different gapped electronic topological phases. The first is called the trivial and the latter the non-trivial phase. At the boundary in parameter space, $w = \mu$, the band gap closes. In fact, one cannot interpolate between the two phases without closing the band gap. This leads to zero-energy modes at domain walls between different phases as well as at the ends of an open non-trivial Kitaev chain. These zero-modes are conjectured to have Majorana character [7] (main text). For the following discussion, we fix the maximal excitation energy of a single Bogoliubon

$$\Lambda := \max(\epsilon_k),\tag{S14}$$

as in the main text.

B. The Dipole Operator

The dipole operator is the sum of the positions of each site times the charge on the same site. For the ring geometry, its x-component reads

$$d_{x} = -eR \sum_{j} \cos\left(\frac{2\pi}{N}j\right) a_{j}^{\dagger} a_{j} = -\frac{eR}{2} \sum_{k} \tilde{a}_{k+1}^{\dagger} \tilde{a}_{k} + h.c.$$

$$= -e \frac{R}{2} \sum_{k} \operatorname{sgn}_{k} \left[\left(c_{k} c_{k+1} - s_{k} s_{k+1} \right) \left(f_{k+1}^{\dagger} f_{k} + f_{k}^{\dagger} f_{k+1} \right) + s_{k} c_{k+1} \left(f_{k+1}^{\dagger} f_{-k}^{\dagger} - f_{k+1} f_{-k} \right) + s_{k} c_{k+1} \left(f_{k+1}^{\dagger} f_{-k}^{\dagger} - f_{k+1} f_{-k} \right) \right],$$

$$+ s_{k} c_{k-1} \left(f_{k-1}^{\dagger} f_{-k}^{\dagger} - f_{k-1} f_{-k} \right) \right],$$
(S15)

where $c_k = \cos(\frac{\vartheta_k}{2})$, $s_k = \sin(\frac{\vartheta_k}{2})$ and $\operatorname{sgn}_k = \operatorname{sgn}(w\cos(\frac{2\pi}{N}k) + \mu)$. Note that Eq. (S15) does not directly follow from Eq. (S10) for $|w| > |\mu|$ (non-trivial phase). We would rather need to replace the terms that cross the inversion points. This leads to new terms

$$eR\left[\left(s_{\lfloor k_{\mathrm{inv}}\rfloor}c_{\lfloor k_{\mathrm{inv}}\rfloor+1} + c_{\lfloor k_{\mathrm{inv}}\rfloor}s_{\lfloor k_{\mathrm{inv}}\rfloor+1}\right)f_{\lfloor k_{\mathrm{inv}}\rfloor+1}^{\dagger}f_{\lfloor k_{\mathrm{inv}}\rfloor} - \left(s_{\lfloor k_{\mathrm{inv}}\rfloor}c_{\lfloor k_{\mathrm{inv}}\rfloor+1} + c_{\lfloor k_{\mathrm{inv}}\rfloor}s_{\lfloor k_{\mathrm{inv}}\rfloor+1}\right)f_{\lfloor -k_{\mathrm{inv}}\rfloor-1}^{\dagger} + \left(c_{\lfloor k_{\mathrm{inv}}\rfloor}c_{\lfloor k_{\mathrm{inv}}\rfloor+1} - s_{\lfloor k_{\mathrm{inv}}\rfloor+1}\right)\left(f_{\lfloor k_{\mathrm{inv}}\rfloor}f_{\lfloor -k_{\mathrm{inv}}\rfloor-1} + f_{\lfloor k_{\mathrm{inv}}\rfloor+1}^{\dagger}f_{\lfloor -k_{\mathrm{inv}}\rfloor}\right)\right],$$
(S16)

where $\lfloor \cdot \rfloor$ is the floor function giving the largest integer smaller than or equal to the argument. We will not consider this technical term any further because for large N this term only has an influence on a null set in k-space.

We go to the interaction picture by replacing $f_i \mapsto f_i(t) = e^{-it\epsilon_j} f_i$. The time-dependent dipole operator reads

$$d_{x}(t) = -e\frac{R}{2} \sum_{k} \operatorname{sgn}_{k} \left[\left(c_{k} c_{k+1} - s_{k} s_{k+1} \right) \left(e^{it(\epsilon_{k+1} - \epsilon_{k})} f_{k+1}^{\dagger} f_{k} + e^{it(\epsilon_{k} - \epsilon_{k+1})} f_{k}^{\dagger} f_{k+1} \right) + s_{k} c_{k+1} \left(e^{it(\epsilon_{k+1} + \epsilon_{k})} f_{k+1}^{\dagger} f_{-k}^{\dagger} - e^{-it(\epsilon_{k+1} + \epsilon_{k})} f_{k+1} f_{-k} \right) + s_{k} c_{k-1} \left(e^{it(\epsilon_{k-1} + \epsilon_{k})} f_{k-1}^{\dagger} f_{-k}^{\dagger} - e^{-it(\epsilon_{k-1} + \epsilon_{k})} f_{k-1} f_{-k} \right) \right].$$
(S17)

Notice that for large N, the coefficients converge to the following functions that can be expressed in simple terms by the system parameters:

$$\operatorname{sgn}_{k}\left(s_{k}c_{k+1}\right)e^{it(\epsilon_{k+1}+\epsilon_{k})} \xrightarrow[N\to\infty]{} \frac{|\Delta|\sin\left(\frac{2\pi}{N}k\right)}{\epsilon_{k}}e^{i2\epsilon_{k}t},\tag{S18}$$

$$\operatorname{sgn}_{k}\left(c_{k}c_{k+1} - s_{k}s_{k+1}\right)e^{it(\epsilon_{k+1} - \epsilon_{k})} \xrightarrow[N \to \infty]{} \frac{2w\cos\left(\frac{2\pi}{N}k\right) + 2\mu}{\epsilon_{k}}.$$
 (S19)

The first coefficient corresponds to increasing or decreasing the number of quasiparticles by two. It is the same (up to a scaling factor Δ) for Hamiltonians with the same band structure. In particular, it will be the same if the topological phases differ, but the band structures coincide, which can happen, see the main text. The second coefficient corresponds to transitions in the same quasiparticle sector. Here, it can be seen that the transition dipole moment has zeroes at the inversion points if and only if the system is in the topologically non-trivial phase. Also notice the different values of the transition energies. For the transitions between quasiparticle sectors, the transition energy is $2E_{\rm Gap} \leq \epsilon_{k+1} + \epsilon_k \leq 2\Lambda$. For transitions within a quasiparticle sector, the transition energy is $|\epsilon_{k+1} - \epsilon_k| \leq \Lambda - E_{\rm Gap}$, and goes to zero for large N. We find that the latter contributions appear in the 2D spectra in the main text as the horizontal peaks. These peaks will have a zero at the energies of the inversion points if and only if the system is in the topologically non-trivial phase. For intermediate and large Δ , this zero splits the peak continuum along the horizontal axis in two parts, as can be seen in the main text. For small Δ , the inversion points are at the lower band edge, so the zero appears at the small frequency end of the horizontal peak continuum. This zero can be identified by comparing with an absorption spectrum or the peaks on the diagonal of the 2D spectrum.

C. Matrix Elements

Here, we provide explicit expressions for the matrix elements for the transitions from the ground state to the two-quasiparticle sector and for transitions within the two-quasiparticle sector.

We denote the quasiparticle vacuum and ground state by $|\Omega\rangle$ and use the convention $|k_1, \ldots, k_n\rangle := f_{k_n} \cdots f_{k_1} |\Omega\rangle$ for $k_1 \leq \cdots \leq k_n$.

1. Groundstate

The groundstate's dipole moment vanishes, i.e.,

$$\langle \Omega | d_x(t) | \Omega \rangle = 0. \tag{S20}$$

2. Groundstate to 2-particle-States

For the transitions from the groundstate to the two-quasiparticle sector, the transition dipole moments are of the form

$$-\frac{2}{eR}\langle k_{1}, k_{2} | d_{x}(t) | \Omega \rangle$$

$$= \sum_{k} \operatorname{sgn}_{k} s_{k} c_{k+1} e^{it(\epsilon_{k+1} + \epsilon_{k})} \langle \Omega | f_{k_{1}} f_{k_{2}} f_{k+1}^{\dagger} f_{-k}^{\dagger} | \Omega \rangle + \sum_{k} \operatorname{sgn}_{k} s_{k} c_{k-1} e^{it(\epsilon_{k-1} + \epsilon_{k})} \langle \Omega | f_{k_{1}} f_{k_{2}} f_{k-1}^{\dagger} f_{-k}^{\dagger} | \Omega \rangle.$$
(S21)

The vacuum expectation values are evaluated by Wick contractions, i.e.,

$$\langle \Omega | f_{k_1} f_{k_2} f_{k+1}^{\dagger} f_{-k}^{\dagger} | \Omega \rangle = \langle \Omega | f_{k_1} f_{k_2} f_{k+1}^{\dagger} f_{-k}^{\dagger} | \Omega \rangle + \langle \Omega | f_{k_1} f_{k_2} f_{k+1}^{\dagger} f_{-k}^{\dagger} | \Omega \rangle$$

$$= -\langle \Omega | f_{k_1} f_{k+1}^{\dagger} f_{k_2} f_{-k}^{\dagger} | \Omega \rangle + \langle \Omega | f_{k_2} f_{k+1}^{\dagger} f_{k_1} f_{-k}^{\dagger} | \Omega \rangle$$

$$= -\delta_{k_1, k+1} \delta_{k_2, -k} + \delta_{k_2, k+1} \delta_{k_1, -k},$$
(S22)

$$\langle \Omega | f_{k_1} f_{k_2} f_{k-1}^{\dagger} f_{-k}^{\dagger} | \Omega \rangle = -\delta_{k_1, k-1} \delta_{k_2, -k} + \delta_{k_2, k-1} \delta_{k_1, -k}.$$
 (S23)

As a result, we obtain

$$\langle k_1, k_2 | d_x(t) | \Omega \rangle = \begin{cases} \frac{eR}{2} \operatorname{sgn}_{k_1} \left(s_{k_1 - 1} c_{k_1} + s_{k_1} c_{k_1 - 1} \right) e^{it \left(\epsilon_{k_1} + \epsilon_{k_1 - 1} \right)}, & \text{if } k_1 + k_2 = 1, \\ \frac{eR}{2} \operatorname{sgn}_{k_1} \left(s_{k_1 + 1} c_{k_1} + s_{k_1} c_{k_1 + 1} \right) e^{it \left(\epsilon_{k_1 + 1} + \epsilon_{k_1} \right)}, & \text{if } k_1 + k_2 = -1, \\ 0, & \text{otherwise.} \end{cases}$$
(S24)

For large N, the only non-vanishing matrix element is

$$\langle k \pm dk, -k | d_x(t) | \Omega \rangle = \operatorname{sgn}_k \frac{eRx_k}{2\sqrt{x_k^2 + 1}} e^{i2\epsilon_k t} = \frac{eR|\Delta|\sin\left(\frac{2\pi}{N}k\right)}{\epsilon_k} e^{i2\epsilon_k t}, \tag{S25}$$

where dk is an infinitesimal shift in momentum space and

$$x_k = \frac{|\Delta| \sin\left(\frac{2\pi}{N}k\right)}{w \cos\left(\frac{2\pi}{N}k\right) + \mu}.$$
 (S26)

In linear spectroscopy, only the absolute squared of the dipole moment in Eq. (S25) enters. The form of the absorption spectra are fully determined by the dispersion relation ϵ_k . If the band structures of two Hamiltonians coincide, they will give rise to the same absorption spectrum modulo a scaling factor of $|\Delta|^2$. Hence, the different topological phases are indistinguishable by linear spectroscopy methods.

3. 2-particle-States to 2-particle-States

Similar as before, the 2-particle to 2-particle transition dipole moments are of the form

$$-\frac{2}{eR}\langle k_1, k_2 | d_x(t) | l_1, l_2 \rangle$$

$$= \sum_k \left(c_k c_{k+1} - s_k s_{k+1} \right) \left(e^{it(\epsilon_{k+1} - \epsilon_k)} \langle \Omega | f_{k_1} f_{k_2} f_{k+1}^{\dagger} f_k f_{l_2}^{\dagger} f_{l_1}^{\dagger} | \Omega \rangle + e^{it(\epsilon_k - \epsilon_{k+1})} \langle \Omega | f_{k_1} f_{k_2} f_k^{\dagger} f_{k+1} f_{l_2}^{\dagger} f_{l_1}^{\dagger} | \Omega \rangle \right),$$
(S27)

with the vacuum expectation values

$$\langle \Omega | f_{k_1} f_{k_2} f_{k+1}^{\dagger} f_k f_{l_2}^{\dagger} f_{l_1}^{\dagger} | \Omega \rangle = \langle \Omega | f_{k_1}^{\dagger} f_{k_2}^{\dagger} f_{k+1}^{\dagger} f_k f_{l_2}^{\dagger} f_{l_1}^{\dagger} | \Omega \rangle + \langle \Omega | f_{k_1}^{\dagger} f_{k_2}^{\dagger} f_{k+1}^{\dagger} f_k f_{l_2}^{\dagger} f_{l_1}^{\dagger} | \Omega \rangle$$

$$+ \langle \Omega | f_{k_1}^{\dagger} f_{k_2}^{\dagger} f_{k+1}^{\dagger} f_k f_{l_2}^{\dagger} f_{l_1}^{\dagger} | \Omega \rangle + \langle \Omega | f_{k_1}^{\dagger} f_{k_2}^{\dagger} f_{k+1}^{\dagger} f_k f_{l_2}^{\dagger} f_{l_1}^{\dagger} | \Omega \rangle$$

$$= \delta_{k_1, k+1} \delta_{k_2, l_2} \delta_{k, l_1} - \delta_{k_1, k+1} \delta_{k_2, l_1} \delta_{k, l_2} - \delta_{k_1, l_2} \delta_{k_2, k+1} \delta_{k, l_1} + \delta_{k_1, l_1} \delta_{k_2, k+1} \delta_{k, l_2},$$

$$(S28)$$

$$\langle \Omega | f_{k_{1}} f_{k_{2}} f_{k}^{\dagger} f_{k+1} f_{l_{2}}^{\dagger} f_{l_{1}}^{\dagger} | \Omega \rangle = \langle \Omega | f_{k_{1}} f_{k_{2}} f_{k}^{\dagger} f_{k+1} f_{l_{2}}^{\dagger} f_{l_{1}}^{\dagger} | \Omega \rangle + \langle \Omega | f_{k_{1}} f_{k_{2}} f_{k}^{\dagger} f_{k+1} f_{l_{2}}^{\dagger} f_{l_{1}}^{\dagger} | \Omega \rangle + \langle \Omega | f_{k_{1}} f_{k_{2}} f_{k}^{\dagger} f_{k+1} f_{l_{2}}^{\dagger} f_{l_{1}}^{\dagger} | \Omega \rangle + \langle \Omega | f_{k_{1}} f_{k_{2}} f_{k}^{\dagger} f_{k+1} f_{l_{2}}^{\dagger} f_{l_{1}}^{\dagger} | \Omega \rangle$$

$$+ \langle \Omega | f_{k_{1}} f_{k_{2}} f_{k}^{\dagger} f_{k+1} f_{l_{2}}^{\dagger} f_{l_{1}}^{\dagger} | \Omega \rangle + \langle \Omega | f_{k_{1}} f_{k_{2}} f_{k}^{\dagger} f_{k+1} f_{l_{2}}^{\dagger} f_{l_{1}}^{\dagger} | \Omega \rangle$$

$$= \delta_{k_{1}, k} \delta_{k_{2}, l_{2}} \delta_{k+1, l_{1}} - \delta_{k_{1}, k} \delta_{k_{2}, l_{1}} \delta_{k+1, l_{2}} - \delta_{k_{1}, l_{2}} \delta_{k_{2}, k} \delta_{k+1, l_{1}} + \delta_{k_{1}, l_{1}} \delta_{k_{2}, k} \delta_{k+1, l_{2}}.$$
(S29)

For large N, it is a good and convenient assumption that $-k \ll k \pm 1$ almost everywhere. Then, the only transition dipole moments relevant for the 2D spectroscopy are

$$\langle k_1, k_2 | d_x(t) | -k, k \pm 1 \rangle = -\frac{eR}{2} \begin{cases} (c_{k_1 - 1}c_{k_1} - s_{k_1 - 1}s_{k_1}) e^{it(\epsilon_{k_1} - \epsilon_{k_1 - 1})}, & \text{if } k_1 = -k + 1 \text{ and } k_2 = k \pm 1, \\ (c_{k_2 - 1}c_{k_2} - s_{k_2 - 1}s_{k_2}) e^{it(\epsilon_{k_2} - \epsilon_{k_2 - 1})}, & \text{if } k_1 = -k \text{ and } k_2 = k + 1 \pm 1, \\ (c_{k_1}c_{k_1 + 1} - s_{k_1}s_{k_1 + 1}) e^{it(\epsilon_{k_1} - \epsilon_{k_1 + 1})}, & \text{if } k_1 = -k - 1 \text{ and } k_2 = k \pm 1, \\ (c_{k_2}c_{k_2 + 1} - s_{k_2}s_{k_2 + 1}) e^{it(\epsilon_{k_2} - \epsilon_{k_2 + 1})}, & \text{if } k_1 = -k \text{ and } k_2 = k - 1 \pm 1. \end{cases}$$
(S30)

For large N, the discussion of the dipole moments is analogous to the one at the end of subsection IV B.

4. 2-particle States to 4-particle States

In a similar way, but with increasing combinatorial effort, the transitions from the two-quasiparticle sector to the four-quasiparticle sector can be obtained. Their effect on the 2D spectra will be similar to what is already discussed at the end of subsection IV B. Representative numerical values are shown in Fig. S6.

V. IDENTIFICATION OF THE TOPOLOGICAL PHASE

Below, we summarize our findings in Secs. III and IV that are relevant for the interpretation of the 2D spectra shown in the main text. The only contributions to the four-point correlation functions in Eqs. (S2) to (S5) come from transitions between the groundstate and two-particle states, from transitions within the two-particle sector, and from

transitions between the two-particle sector to the four-particle sector. As seen from Figs. S4 and S6, the transition dipole moments from the ground state to two-particle states and the transition dipole moments from two-particle to four-particle states show no qualitative difference for Hamiltonians with the same dispersion relation. In fact, they merely differ by a scaling factor that is the ratio between the supeconducting gap parameters of the two Hamiltonians $|\Delta'|/|\Delta|$ as derived in subsection IV B. We observe in the numerical computations in Figs. S4 and S6 that the scaling factors are in agreement with $|\Delta'|/|\Delta| = 99$ for s = 0.01 and s' = 0.99, and $|\Delta'|/|\Delta| = 3$ for s = 0.25 and s' = 0.75. This scaling factor is fully determined by the condition that the band structures coincide and the topological phases differ as seen in Eq. (2) of the main text. Yet, such a scaling factor is not a conclusive signature which characterizes the topological phases in a unique way. Instead a qualitative difference in the 2D spectra of the topological phases stems from the transitions within the two-particle sector. For these transitions, we observe differences in Fig. S4, in particular, a cluster of transitions with close-to-zero dipole moments in the non-trivial phase that is absent in the trivial phase. We characterize these zeroes by the analytic result in subsection IVB. Eq. (S19) and show that the two-to-two-particle transition dipole moments are always finite in the trivial phase but cross zero in the non-trivial phase. The crossing from negative to positive occurs precisely at the inversion points in k-space where the band changes from a predominantly particle to a predominantly hole band. Hence, these zeroes are a consequence of the band inversion happening in the non-trivial phase. In the spectra, the transitions within the two-particle sector appear as low-frequency transitions while the transitions that change the number of quasiparticles must overcome at least twice the band gap. Therefore, the contributions that are characteristic for a topological phase should appear on the horizontal of the 2D spectra. There, they section the continuum in two precisely at the energy of the inversion points as seen in Fig. 1c in the main text. For small Δ , i.e., $|\Delta|^2 < w^2 - \mu^2$, this energy is found at the lower band edge and is only identifiable by comparison with linear spectra or the diagonal of the 2D spectrum.

VI. SPECTROSCOPY OPERATOR OF THE RASHBA WIRE

The Kitaev chain is the archetype of one-dimensional topological superconductors. However, it only appears in nature as a low-energy description of specifically engineered mesoscopic systems that require auxiliary effects such as proximity-induced superconductivity, spin-orbit coupling and strong magnetic fields. The general form of the spectroscopy operator given by the projection of the dipole operator onto the low-energy theory is a priori unclear. In this section, we demonstrate that the spectroscopy operator as given in the main text is the principal contribution to the spectroscopy operator of a semiconducting wire.

The Rashba wire is conjectured to realize topological superconductivity. It is a semiconducting wire on an s-wave superconducting substrate with strong spin-orbit coupling and Zeeman splitting due to applied external magnetic fields. It was first realized in an experiment reported in Ref. [12]. Following the exposition in Ref. [11], we derive its spectroscopy operator for the low-energy band in the limit of large magnetic fields B. The Hamiltonian of the Rashba wire is

$$H = \int dx \left[\left(\psi_{\uparrow x}^{\dagger}, \ \psi_{\downarrow x}^{\dagger} \right) \left(-\frac{\hbar^2 \partial_x^2}{2m} - \mu - i\hbar u (\mathbf{e} \cdot \boldsymbol{\sigma}) \partial_x - \frac{g\mu_B B_z}{2} \sigma^z \right) \left(\psi_{\downarrow x}^{\dagger} \right) + \left(\Delta \psi_{\downarrow x} \psi_{\uparrow x} + \text{h.c.} \right) \right], \tag{S31}$$

where $\mathbf{e}=\left(e_x,\ e_y,\ 0\right)$ with $e_x^2+e_y^2=1$. Further, μ is the chemical potential, u the Dresselhaus/Rashba spin-orbit coupling strength and $\boldsymbol{\sigma}$ the vector of Pauli matrices. The spin-singlet pairing Δ is due to proximity to an s-wave superconducting substrate. For large magnetic fields, one can project the Hamiltonian onto a single-band model [11]. If $g\mu_B|B_z|\gg\mu$ and $g\mu_B|B_z|\gg|\Delta|$, then $\psi_{\uparrow x}\sim\frac{\hbar u(e_x+ie_y)}{g\mu_B|B_z|}\partial_x\Psi_x$ and $\psi_{\downarrow x}\sim\Psi_x$. The low-energy Hamiltonian is

$$H \sim \int dx \left[\Psi_x^{\dagger} \left(-\frac{\hbar^2 \partial_x^2}{2m} - \mu_{\text{eff}} \right) \Psi_x + (\Delta_{\text{eff}} \Psi_x \partial_x \Psi_x + \text{h.c.}) \right],$$
 (S32)

with $\mu_{\text{eff}} = \mu + g\mu_B |B_z|/2$ and

$$\Delta_{\text{eff}} \approx \frac{\hbar u \Delta}{g \mu_B |B_z|} (e_x + i e_y).$$
 (S33)

We proceed to express the dipole operator in terms of the field operator Ψ_x . The dipole operator is

$$\mathbf{d} = -e \int dx \, \mathbf{r}_x \left(\psi_{\downarrow x}^{\dagger} \psi_{\downarrow x} + \psi_{\uparrow x}^{\dagger} \psi_{\uparrow x} \right), \tag{S34}$$

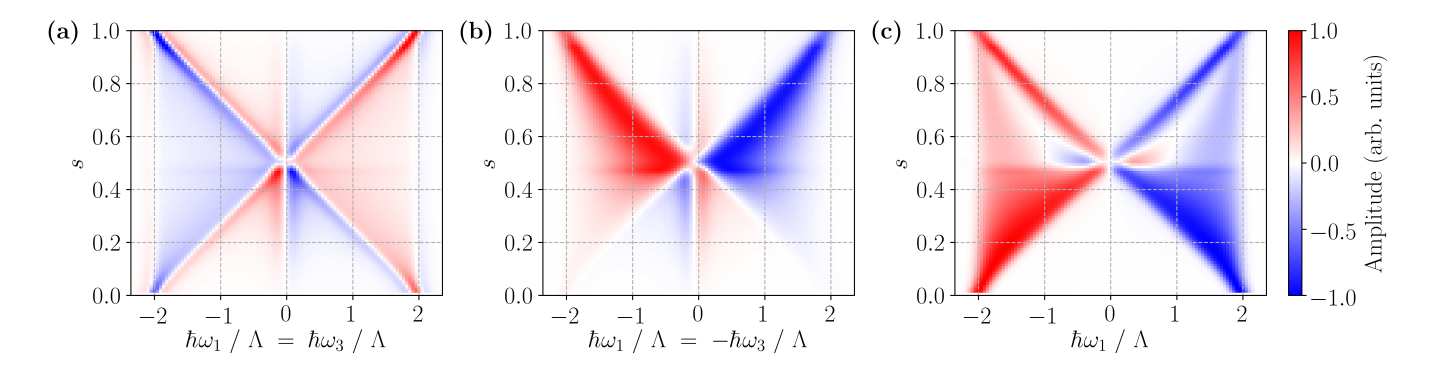


FIG. S7. (a) Diagonal, (b) counterdiagonal and (c) horizontal sections of the imaginary part of the 2D spectra for the lattice Hamiltonian of the Rashba wire $H_{\text{Lattice}}(w_L, \mu_L, \Delta_L) = H_{\text{Lattice}}(s\Lambda/2, (1-s)\Lambda/2, s\Lambda/2)$ as a function of s in analogy with Fig. 3 in the main text. The dipole operator is given by Eq. S40 with $\Delta = \Lambda$. For each s, the 2D spectra are normalized to their maximal peak amplitude. The chain length is N = 60. For s < 0.5, the chain is in the trivial phase, and for s > 0.5, the chain is in the non-trivial phase. Compared to the results for the pure Kitaev model, we observe only little difference. There is only a slight fading of the high-frequency peaks on the horizontal.

where \mathbf{r}_x denotes the physical position at x. Here, we consider x to merely parametrize the one-dimensional chain and not to distinguish any spatial direction. Projecting the dipole operator onto the low-energy band yields

$$\mathbf{d} \sim -e \int dx \, \mathbf{r}_x \Psi_x^{\dagger} \Psi_x - \frac{2emu^2}{\hbar^2 q^2 \mu_D^2 |B_z|^2} \int dx \, \mathbf{r}_x \Psi_x^{\dagger} \left(-\frac{\hbar^2 \partial_x^2}{2m} \right) \Psi_x. \tag{S35}$$

We can already see here that the principal term is of the same kind as for the dipole operator given in the main text and the additional hopping term is negligible for sufficiently large B-fields.

In order to compare these results to the results for the Kitaev chain, we need to fit this continuum model to a lattice model. We arrive at the Kitaev Hamiltonian

$$H_{\text{Lattice}} = \sum_{n=1}^{N} \left[-w_L a_{n+1}^{\dagger} a_n - \mu_L a_n^{\dagger} a_n + \Delta_L a_n a_{n+1} \right] + \text{h.c.}$$
 (S36)

with the hopping parameter w_L , the chemical potential μ_L and the p-wave pairing term Δ_L given by

$$w_L = \frac{\hbar^2}{2m\lambda^2} \,, \tag{S37}$$

$$\mu_L = \frac{\mu_{\text{eff}}}{2} - \frac{\hbar^2}{2m\lambda^2} = \frac{\mu}{2} + \frac{g\mu_B|B_z|}{4} - \frac{\hbar^2}{2m\lambda^2},$$
 (S38)

$$\Delta_L = \frac{\Delta_{\text{eff}}}{\lambda} = \frac{\hbar u \Delta}{\lambda g \mu_B |B_z|} (e_x + i e_y). \tag{S39}$$

Here, λ is the lattice constant. We introduce the spin-orbit coupling energy $E_{\text{SOC}} = \hbar u/\lambda$ and the Zeeman energy $E_{\text{Zeeman}} = g\mu_B |B_z|$. Within this lattice fit the final spectroscopy operator reads

$$\mathbf{d}_{\text{Lattice}} = -e \sum_{n} \mathbf{r}_{n} a_{n}^{\dagger} a_{n} - e \frac{\left|\Delta_{L}\right|^{2}}{\left|\Delta\right|^{2}} \sum_{n} \mathbf{r}_{n} \left(a_{n+1}^{\dagger} a_{n} + a_{n}^{\dagger} a_{n+1}\right)$$
(S40)

$$= -e \sum_{n} \mathbf{r}_{n} a_{n}^{\dagger} a_{n} - e \frac{E_{\text{SOC}}^{2}}{E_{\text{Zeeman}}^{2}} \sum_{n} \mathbf{r}_{n} \left(a_{n+1}^{\dagger} a_{n} + a_{n}^{\dagger} a_{n+1} \right). \tag{S41}$$

The first term corresponds to the spectroscopy operator in the main text. The additional hopping-like term is suppressed by the ratio of the spin-orbit coupling to the Zeeman energy squared. Equivalently, the prefactor is given by the ratio of the p-wave gap in the lattice model to the proximity-induced s-wave gap of the overall wire. In a typical experimental setup this term is at most of the order of a few percent [12]. Such minor terms are negligible in nonlinear spectroscopy. To demonstrate the influence of this term, we have repeated the calculation of the 2D spectra for the same parameters as used for Fig. 3 of the main text. In this setup, the prefactor of the hopping-like

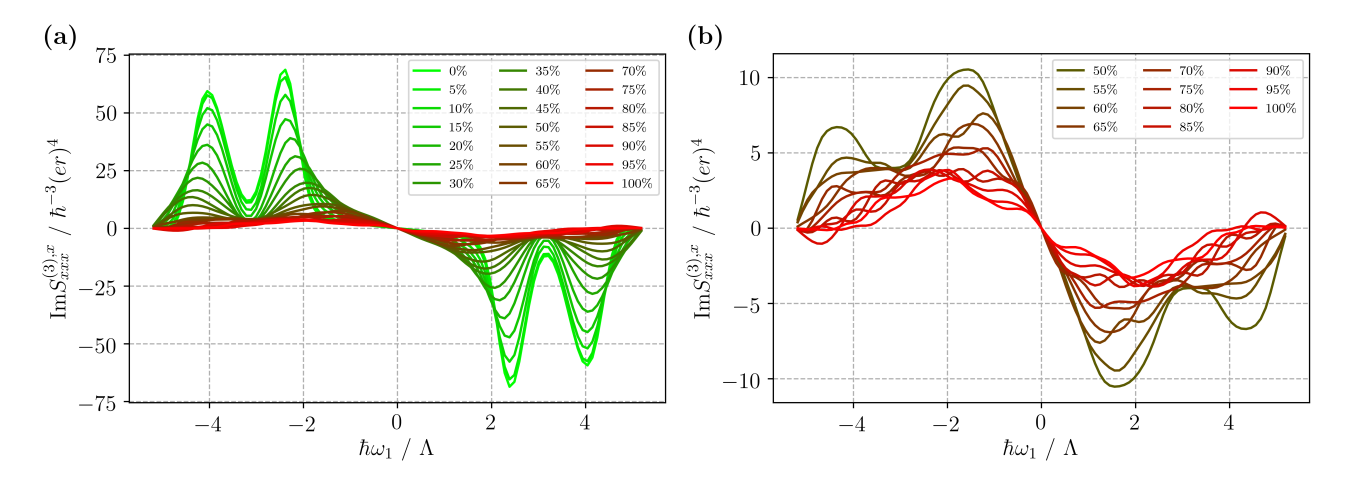


FIG. S8. Horizontal sections of the 2D spectra of the Kitaev ring in its topological phase for varying degrees of local parametric disorder, see Eq. S42. (a) The sections are depicted for different disorder strengths increasing from 0% to 100% of the band gap energy with step sizes of 5%. Each averaged over 100 samples. Even for significant disorder, the peak splitting on the horizontal remains distinguishable, serving as unique identifier of the topological phase. (b) The disorder strengths α from 50% to 100% of the band gap energy are highlighted. The peak splitting vanishes, ruling out the possibility to identify the topologically nontrivial phases at large disorder.

contribution varies since we vary Δ_L . We choose $\Delta = \Lambda$. In the topological phase, i.e., s > 0.5, the prefactor ranges from 6.25 % to 25 %. Thus, it is with our intentionally unrealistic choice of Δ one order of magnitude larger than to be expected. The result is shown in Fig. S7. We observe no qualitative deviations from the results of the main text. There is merely a fading of the high-frequency peaks along the horizontal. Yet, the peak splitting remains clearly visible.

VII. DISORDER

In this section, we want to exemplify the effect of disorder on the characteristic signatures of the 2D spectra discussed in the main text. Therefore, we add parametric local disorder to the Hamiltonian in the the cases s = 0.25 (trivial phase) and s = 0.75 (topological phase) as depicted in Fig. 1a and c in the main text. We accomplish this by adding random variables w_n , μ_n and Δ_n drawn uniformly from [-1,1] to each parameter at every site or bond, respectively.

$$H_{\text{disorder}}(w,\mu,\Delta;\alpha) = \sum_{n=1}^{N} \left[-(w+\alpha w_n) a_{n+1}^{\dagger} a_n - (\mu+\alpha\mu_n) a_n^{\dagger} a_n + (\Delta+\alpha\Delta_n) a_n a_{n+1} \right] + \text{h.c.}$$
 (S42)

Here, α quantifies the strength of the disorder. Again, periodic boundary conditions are imposed, i.e., $a_{N+1}=a_1$. To determine the influence of disorder on the separation of the horizontal peaks of the 2D spectra, we vary α from 0 to the band gap energy, which is in both cases 0.5Λ and average the results over 100 samples. The results for the topological and trivial phase are shown in the Supplemental Movies 2 and 3, respectively, where increasing time corresponds to increasing α . Increasing the disorder strength mostly result in a narrowing of the band gap and in a peak broadening additional to the method-related initial one. We observe that the signature of the topological phase, namely the peak-splitting on the horizontal ($\omega_3=0$) axis of the 2D spectra, remains clearly visible up to values of α about 30% of the band gap but mostly vanishes at 50% of the band gap energy. Sections of the horizontal peaks in the 2D spectra of the topological are depicted in Fig. S8. For the trivial phase, we only observe the aforementioned generic consequences of disorder, peak broadening and closure of the excitation gap. As the Supplemental Movies 2 and 3 show, both phases eventually approach the same 2D spectrum for large disorder strengths. The distinction of the two phases by the splitting of the horizontal peaks remains possible until a disorder strength of at least 30%, as shown in Figs. S8 and S9. We hence conclude that the described method of identifying one-dimensional superconductivity by unique features in the 2D spectra, remains viable up to significant parametric disorder.

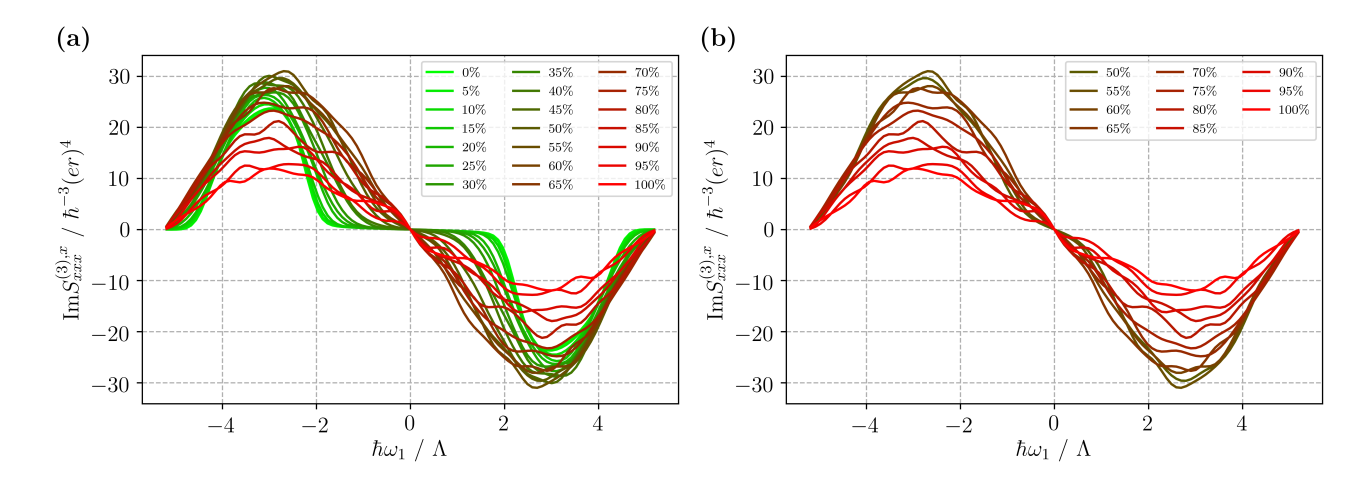


FIG. S9. Horizontal sections of the 2D spectra of the Kitaev ring in its trivial phase for varying degrees of local parametric disorder, see Eq. S42. (a) The sections are depicted for different disorder strengths increasing from 0% to 100% of the band gap energy with step sizes of 5%. Each averaged over 100 samples. (b) The disorder strengths α from 50% to 100% of the band gap energy are highlighted. The increasing disorder strength mostly causes peak broadening and the closure of the band gap.